Microstructure-properties relation of hydrostatically extruded absorbable zinc alloys

Effect of Mg and Cu addition on corrosion properties and biocompatibility

Jarzębska, Anna; Gieleciak, Magdalena; Bigos, Agnieszka; Maj, Łukasz; Trembecka-Wójciga, Klaudia; Bugajska, Monika; Bieda, Magdalena; Rogal, Łukasz; Kawałko, Jakub; Przybysz, Sylwia

Total number of authors:
13

Published in:
Journal of Materials Research and Technology

Link to article, DOI:
10.1016/j.jmrt.2024.03.044

Publication date:
2024

Document Version
Publisher's PDF, also known as Version of record

Journal of Materials Research and Technology 30 (2024) 283–294

Contents lists available at ScienceDirect

Journal of Materials Research and Technology

journal homepage: www.elsevier.com/locate/jmrt

Microstructure-properties relation of hydrostatically extruded absorbable zinc alloys: Effect of Mg and Cu addition on corrosion properties and biocompatibility

Anna Jarzębska [a,1,*], Magdalena Gieleciak [a,1], Agnieszka Bigos [a], Łukasz Maj [a], Klaudia Trembecka-Wójciga [a,b], Monika Bugajska [a], Magdalena Bieda [a], Łukasz Rogal [a], Jakub Kawałko [c], Sylwia Przybysz [d], Daniel Wojtas [a,e,f], Aldona Mzyk [f,g], Romana Schirhagl [f]

[a] Institute of Metallurgy and Materials Science, Polish Academy of Sciences, Krakow, Poland
[b] Department of Biotechnology and Physical Chemistry, Faculty of Chemical Engineering and Technology, Cracow University of Technology, Krakow, Poland
[c] Academic Centre for Materials and Nanotechnology, AGH University of Krakow, Poland
[d] Institute of High Pressure Physics, Polish Academy of Sciences, Warszawa, Poland
[e] Faculty of Medicine, Masaryk University, Brno, Czech Republic
[f] Department of Biomedical Engineering, Groningen University, University Medical Center Groningen, Groningen, Netherlands
[g] Department of Health Technology, Danish Technical University, Kongens Lyngby, Denmark

ARTICLE INFO

Handling editor: P.Y. Chen

Keywords:
Absorbable zinc alloys
Hydrostatic extrusion
Corrosion behavior
Cytotoxicity of zinc alloys

ABSTRACT

Pure Zn is well-known for its appropriate corrosion rate, making it suitable for use as future absorbable implants. Yet, it suffers from insufficient strength, thus, both plastic deformation and alloying are required. Hydrostatic extrusion has proven to be an efficient technique, providing high mechanical properties for zinc alloys. However, its effect on degradation rate and biocompatibility of Zn alloys remains unknown. Thus, within the present study, an attempt to evaluate those properties has been made on hydrostatically extruded pure Zn, Zn–Mg and Zn–Mg–Cu alloys. The materials were characterized by advanced microscopy techniques and uniaxial tensile tests. Corrosion properties were assessed based on electrochemical and static immersion tests. Finally, the cytotoxic effect of zinc extracts on endothelial cells were examined by standard MTT assays combined with confocal imaging.

The results showed that hydrostatic extrusion results in significant refinement of α-Zn grains and the intermetallic phase Mg_2Zn_{11} for the investigated alloys. The alloys exhibited ultimate tensile strength exceeding 300 MPa and elongation higher than 20%. Corrosion tests demonstrated that all the materials showed a similar level of degradation rate. Moreover, the uniform distribution of the intermetallic phase contributed to homogeneous corrosion of Zn alloys. Biological studies indicated that the least cytotoxic response in endothelial cells was obtained for the Zn–Mg alloy. Such an effect was caused by the limited amount of released Zn ions in the favor of Mg ions.

The refinement of α-Zn grains and intermetallic phases caused by hydrostatic extrusion were key factors determining the performance of Zn-based materials.

1. Introduction

The right method to improve the mechanical properties of pure zinc is of great importance since they are the bottleneck for biomedical applications, e.g., as absorbable cardiovascular stents [1]. Unlike magnesium and iron, zinc is characterized by an optimal corrosion rate, making it a promising candidate for a new generation of absorbable implants. Moreover, zinc is an essential element in the human body, involved in a vast number of biological functions like cell growth, DNA formation or protein synthesis [2]. Therefore, on many different levels zinc is attractive for the production of temporary implants, once its mechanical properties are improved. Alloying with various elements is

* Corresponding author.
E-mail address: a.jarzebska@imim.pl (A. Jarzębska).
[1] These authors contributed equally.

https://doi.org/10.1016/j.jmrt.2024.03.044
Received 24 October 2023; Received in revised form 28 January 2024; Accepted 7 March 2024
Available online 8 March 2024

the most common approach for strengthening zinc. Depending on the chosen element, different improvements can be obtained. In the case of absorbable stents, providing high strength of a material is not sufficient as high ductility is necessary too [3]. Zn–Mg and Zn–Li alloys belong to the group of high-strength materials, while Zn–Mn and Zn–Cu alloys are high ductility materials [4]. Thus, creating multicomponent alloys is a promising strategy increasing both strength and ductility [5,6].

As the criteria imposed on absorbable implants are very demanding [3], alloying itself may be insufficient and needs to be supported by plastic deformation [7]. A remarkable increase in both strength and plasticity can be obtained by using severe plastic deformation (SPD) processes like equal channel angular pressing (ECAP) or high-pressure torsion (HPT). So far, room-temperature ECAP led to one of the highest mechanical properties ever reported for low-alloyed zinc (Zn-0.1 Mg) i.e., yield strength (YS) of 329 MPa, ultimate tensile strength (UTS) of 383 MPa and elongation of 45.6% [8]. An even more spectacular improvement has been obtained with HPT applied to Zn–1Mg as it yielded YS of 374 MPa, UTS of 459 MPa and elongation of 6.3% [9]. Another very effective technique of enhancing mechanical properties of Zn–Mg alloys is hydrostatic extrusion (HSE), an unconventional SPD method. Due to the triaxial stress state provided by the surroundings of a pressurized medium, it is possible to deform materials at high speed and at room temperature, which positively affects microstructural features. The fact that the billet is surrounded by a medium and pushed through the die, not by a punch itself, helps minimize friction between the parts. This in turn promotes high deformation to be obtained and differs the technique from conventional extrusion [10]. Pachla et al. showed that by optimizing HSE parameters and chemical composition of the zinc alloys various mechanical properties can be obtained. For instance, the Zn-0.5 Mg alloy hydrostatically extruded in the four consecutive passes reached UTS of 514 MPa, with 10.5% of elongation, while in the case of the Zn-1.5 Mg alloy, deformed in the same way, UTS of 463 MPa and elongation of 38.6% were achieved [11]. The authors also presented, that lowering the numbers of deformation passes to two resulted in decreasing of strength of the materials, regardless of the chemical composition. Meanwhile, the plasticity of the zinc-based materials was improved. Thus, three passes of HSE were applied in present work to obtain compromise between optimal strength and plasticity of zinc alloys.

Improvement in strength and plasticity during HSE is ascribed to substantial microstructural changes. Significant refinement of α-Zn phase even up to 700 nm [12] and eutectic mixture to the nanoscale [10] are the main cause of strengthening of Zn–Mg alloys processed by HSE. Moreover, redistribution of the intermetallic phase into elongated bands and the creation of composite-like microstructure are crucial factors inducing to the improvement in mechanical properties. Another important feature is that HSE induces to creation of structural defects, which also take part in strengthening of the materials. Apart from substantial microstructural refinement of the Zn–Mg alloys, the HSE also leads to the formation of a unique crystallographic texture, making deformation with secondary slip systems possible. As a result, higher plasticity of materials is achieved as seen for Zn–Mg alloys [10–12]. Such notable microstructural changes are difficult to obtain by commonly applied methods of plastic deformation, like hot extrusion or hot rolling [13]. It is due to the fact that such techniques are limited in providing large amount of plastic strain [13]. In the case of the Zn–Mg alloys deformed via conventional processes, grain size is usually in the range of 10–50 μm [14]. In order to further reduce the grain size, the addition of another alloying elements or application of cold deformation processes are needed. For example, Wang et al. showed that Zn-0.02 Mg alloy obtained by hot extrusion with subsequent multi-pass drawing at room temperature can result in grain size of 1 μm [15]. Similar results were also achieved for Zn–5Cu processed by hot extrusion with subsequent cold rolling up to 90% [16].

The microstructural refinement not only strengthens the material but can also affect its other properties including corrosion resistance or biocompatibility [17]. It is believed that, in the environment which facilitates material oxidation, grain refinement can promote the formation of an oxide layer, improving corrosion resistance [18]. Ye et al. [19] indicated that grain refinement which occurred in the Zn-0.3 Mg alloy may delay ion diffusion and in consequence decrease its degradation rate. Besides, in Zn-0.5Mn alloys grain refinement may suppress localized corrosion and lead to uniform degradation [20]. In the same work, the authors showed that an implant having refined microstructure was characterized by satisfactory histocompatibility and no inflammation or damage of rat liver and kidney were observed. The other microstructural features i.e., secondary phases, may result in micro-galvanic corrosion and initiate the degradation processes [21]. However, Guillory et al. showed that a uniform distribution of fine Mn/Zr-rich intermetallic phases may bring about more homogenous degradation of the multicomponent zinc alloys. Moreover, the authors also believed that this correlates with superior biological response as tailoring microstructure in terms of chemical composition might decrease the cytotoxicity effect of zinc-based materials on cells. The quinary alloy the authors developed exhibited superior biocompatibility than binary alloys, since reduced neointimal growth and a more uniform biological response during *in vivo* studies were observed [22].

Considering the possibilities of microstructure refinement down to the sub-micron scale by hydrostatic extrusion as compared to the conventional methods of plastic deformation, it is crucial to investigate its impact on the functional properties of zinc alloys with potential biomedical applications. Therefore, the goal of this work was to study the effect of alloying of HSE-treated Zn-based materials on their corrosion behaviour and cytotoxicity with simultaneous correlation with the microstructure. The initial attempts to evaluate in vitro degradation rate based on static immersion as well as electrochemical tests and cytotoxicity with the use of MTT assay supported with confocal imaging were made by investigating pure Zn and two different alloys – binary with Mg addition and ternary containing Mg and Cu.

2. Experimental procedure

2.1. Materials preparation

In this study, pure Zn and two alloys, Zn–Mg and Zn–Mg–Cu were investigated. The materials were obtained by melting high-purity zinc, magnesium (99.99%) and M60 brass at 650 °C under argon atmosphere and subsequently cast into steel moulds. The resulting as-cast pure Zn, Zn–Mg (0.8 wt % of magnesium) and Zn–Mg–Cu (0.8 wt % of magnesium and 0.2 wt % of copper) were subjected to hot extrusion at 250 °C with a reduction (R) of 5.8. Finally, the materials were processed by multi-pass HSE realized in three consecutive steps at room temperature, resulting in a cumulative true strain ε of 3.6. The materials were comprehensively studied to analyze the effect of SPD on microstructure, mechanical properties, corrosion properties as well as biological properties. Fig. 1 shows schematic diagram of the materials preparation for further investigations.

2.2. Microstructural characterization

To investigate microstructure changes triggered by plastic deformation, the Electron Backscattered Diffraction (EBSD) technique was implemented by using a FEI Quanta 3D FEG scanning electron microscope. Sample surfaces were prepared by grinding up to 7000 gradation abrasive papers, followed by polishing with diamond suspensions, and finally, electropolished. EBSD scan sizes were individually adjusted for each material to ensure appropriate grain statistics. In the case of pure Zn, a step size of 0.2 μm and a map size of 250 μm × 250 μm were chosen. For alloys, a step size and a map size of 0.075 μm and 85 μm × 85 μm, respectively, were selected. Microstructural analysis, encompassing information about grain size, grain boundary density was provided from the longitudinal cross-sections to the extrusion direction

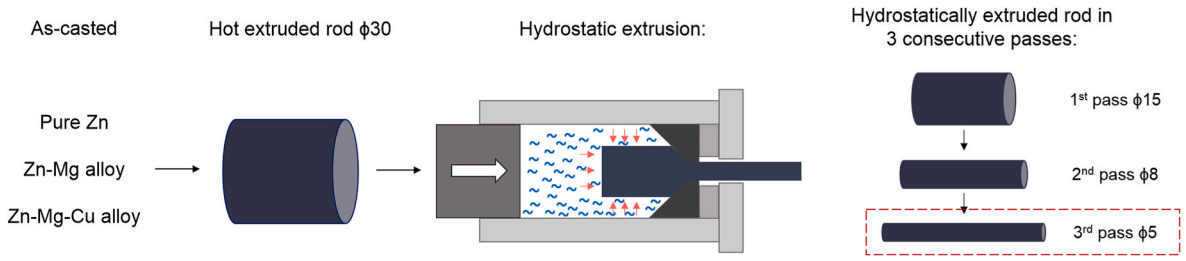

Fig. 1. Schematic diagram of sample preparation.

(ED). The EBSD data was analyzed using Matlab and MTEX toolbox. For the purpose of the grain size, and grain boundary density analysis, the EBSD data was filtered to remove incorrectly indexed data points, associated mostly with areas of intermetallic phase, or pattern overlap at grain boundaries. Grain reconstruction was carried out on the assumption that a grain is represented by a cluster of measurement points, surrounded by the boundary segments with misorientation angle of at least 15°. Clusters composed of less than 5 points were removed before further analysis. The grain size analysis was carried out using the above grain definition. The grain diameter was estimated as the diameter of a circle with equivalent surface area. Reported average grain diameters and standard deviations, are area weighted. The weights for average, and standard deviation values were calculated as surface area of grain, divided by total surface area of all grains after data filtering. For the grain boundary analysis, a grain boundary segment was defined as linear boundary segment between two indexed data points with misorientation angle of at least 2°, and length equal to $s/\sqrt{3}$, where s is the step size in a hexagonal grid map. Boundary segments with misorientation angle of at least 15° were classified as high angle grain boundaries (HAGB), and boundary segments with misorientation angle below 15° were classified as low angle grain boundaries (LAGB). Boundary density was calculated as total length of given boundary type divided by a total surface area represented by the analyzed EBSD scan.

Nanoscale observations were performed with a ThermoFisher Titan Themis G2 200 Probe Cs-Corrected transmission electron microscope (TEM) equipped with CetaTM CCD camera for the acquisition of microstructure images and electron diffraction patterns, Fishione HAADF/STEM detector and ChemiSTEM system for chemical analysis (EDS method). Prior to TEM observations, a set of thin foils from the longitudinal cross-sections was carefully prepared. In doing so, electropolishing in 5% $HClO_4$ mixed with methanol was realized. The investigated materials were also the subject of TEM-assisted phase analysis and chemical analysis. The former was carried out through indexing of the SAED patterns with CSpot software [23], whereas the latter was conducted with the help of the Velox software.

2.3. Mechanical properties

The mechanical behavior of the materials was assessed by a series of uniaxial tensile tests performed by using a Zwick/Roell Z250 kN machine. Three cylindrical samples from each of the studied materials were tested. They were 3 mm in diameter and had a gauge length of 15 mm. During tension, a constant strain rate of 1×10^{-3} $s^{-1}$was maintained.

2.4. Corrosion properties

The electrochemical tests were used first to determine the corrosion rate of the investigated materials. These tests were performed with the use of an AUTOLAB PGSTAT302 N potentiostat/galvanostat and controlled with the commercial NOVA 2.1.4 software. The electrochemical measurements were carried out in c-SBF solution, mimicking blood plasma [24], at 37 °C in a Pine thermostatic cell, using a standard three-electrode system. The system consisted of a working electrode - investigated material, a reference electrode - a saturated calomel electrode (SCE) (placed in a Luggin capillary), and platinum auxiliary electrodes. The working area of the samples equalled approximately 0.2 cm^2 and was prepared by grinding with the use of SiC-based papers up to 7000 gradation and then polishing with diamond suspensions. The open-circuit potential (OCP) was measured as a function of time during 3600 s in order to obtain a stable value. Subsequently, the polarization measurements were carried out at a scan rate of 0.001 V/s, ranging from −120 mV to +120 mV with respect to the corrosion potential (E_{corr}). The corrosion rates were estimated by extrapolating the polarization curves according to the ASTM-G102-89 standard. The measurements were repeated at least five times to guarantee the data precision. The corrosion rates were computed from the corrosion current density using the following formula:

$$CR = 3.27 \bullet 10^{-3} \frac{i_{corr} EW}{\rho}$$

where CR is the corrosion rate (mm•$year^{-1}$), i_{corr} is the corrosion current density (μA•cm^{-2}), EW is the equivalent weight of a metal (32.7 for pure zinc) and ρ is the material density (g•cm^{-3}).

Additionally, the corrosion rate was supported by static immersion tests performed for 336 h. The exposed surface of the immersed samples was ground on abrasive papers up to 7000 gradation. Subsequently, the samples were ultrasonically cleaned in n-Hexane, acetone and ethanol, dried in air and weighted. The prepared samples with the volume-to-sample area ratio equal to 50 mL•cm^{-2}, were immersed in c-SBF solution at 37 °C. In order to keep the pH value constant around 7.4, the medium was refreshed every two days. After 336h of immersion, the samples were washed with distilled water, dried in air and subjected to corrosion product removal with chromic acid (180 g•L^{-1}) for 10 min and then their mass loss was weighted. Based on the mass loss, the corrosion rates were calculated according to following formula:

$$CR = 8,76 * 10^4 \frac{(m_s - m_f)}{St\rho}$$

where CR is the corrosion rate (mm•$year^{-1}$), m_s (g) is the sample mass prior to immersion, m_f (g) is the sample mass after immersion and removal of corrosion products, S (cm^2) is the sample area exposed to c-SBF, t (h) is the immersion time and ρ (g•cm^{-3}) is the material density. From each material 9 samples were prepared, among which 6 were used for calculating CR average value and 3 were taken for further observation of corrosion products.

The corrosion products were characterized through the cross-sectional observations and mapping of chemical elements with the use of ThermoFisher Scios 2 Dual Beam electron microscope equipped with a ThermoFisher EDS detector. A Ga + ion beam was used for sputtering and final polishing of both the substrate material and layer of corrosion products to secure the proper condition for imaging and elemental mapping. The EDS maps were collected with the use of accelerating voltage of 10 kV.

2.5. Biological properties

Biocompatibility of investigated samples was evaluated according to

the ISO 10993–5:2009. Human umbilical vein endothelial cells (HUVECs, CC2519, Lonza) obtained by courtesy of the UMCG Endothelial Cell Facility were used for in vitro cytotoxicity analysis of all the investigated materials. EGM-2MV solution (CC3202, Lonza), consisting of EBM-2 basal medium (CC3156, Lonza), supplements as well as growth factors (CC4147, Lonza) was used for HUVECs culturing. The cells were incubated at 37 °C in a humified atmosphere of 5% CO_2/95% air until 90% confluency was reached. Indirect contact cytotoxicity studies were carried out to evaluate how zinc and its alloys affect HUVECs. In doing so, the so-called extracts i.e., cell culture media containing ions that have diffused from the surface of a specific material were tested. The extracts were prepared by placing fresh medium onto samples at a ratio of 1.25 ml/cm^2 and their subsequent 24-h incubation at 37 °C and 5% CO_2. Then, solutions were harvested and stored at −20 °C until further use. Even though three different materials are described within the present study, henceforth we only use the term "zinc extracts".

The standard MTT assay was performed to determine the metabolic activity of zinc extracts-treated HUVECs. The cells were seeded in a 96-well plate at the density of 2.1 × 10^4 cells/ml and incubated for 24 h at 37 °C and 5% CO_2. Consequently, they were immersed in the collected extracts and incubated anew for 4 h. Each of the extracts was tested in six replicates and the cells cultured in normal medium i.e., without any extract additions, were regarded as the negative control. Upon incubation, the MTT (3-(4,5-dimethylthiazol-2-yl)-2,5-diphenyltetrazolium bromide) dissolved in the culture medium at a concentration of 5 mg/ml was poured onto HUVECs and incubated at 37 °C and 5% CO_2 for additional 3 h. Afterwards, the MTT-containing medium was decanted as dimethyl sulfoxide (DMSO) was put in each of the wells. Finally, the plate was gently and quickly shaken, and a microplate reader (Biotek Instruments) was used to measure the spectrophotometric absorbance at 570 nm. The results were referenced to the negative control and expressed as percentage metabolic activities.

The MTT assay was additionally supported by confocal laser scanning microscopy (CLSM) studies. For this purpose, HUVECs were first seeded onto 12-well plates at a density of 1 × 10^5 cells/ml and incubated at 37 °C and 5% CO_2. When confluent, they were immersed in extracts and incubated again for 4 h. Then, the cells were washed with phosphate buffered saline (PBS) and fixed with 4% (wv-1) paraformaldehyde solution for 10 min. Subsequently, 1 mg/ml DAPI (Sigma) and 2 mg/ml FITC-phalloidin (Sigma) were employed to stain nuclei and actin. Afterwards, all of the wells were flushed with PBS and imaged by using a Stellaris 8 Leica Microsystems. In doing so, a series of at least 6 images taken for all of the investigated groups was captured.

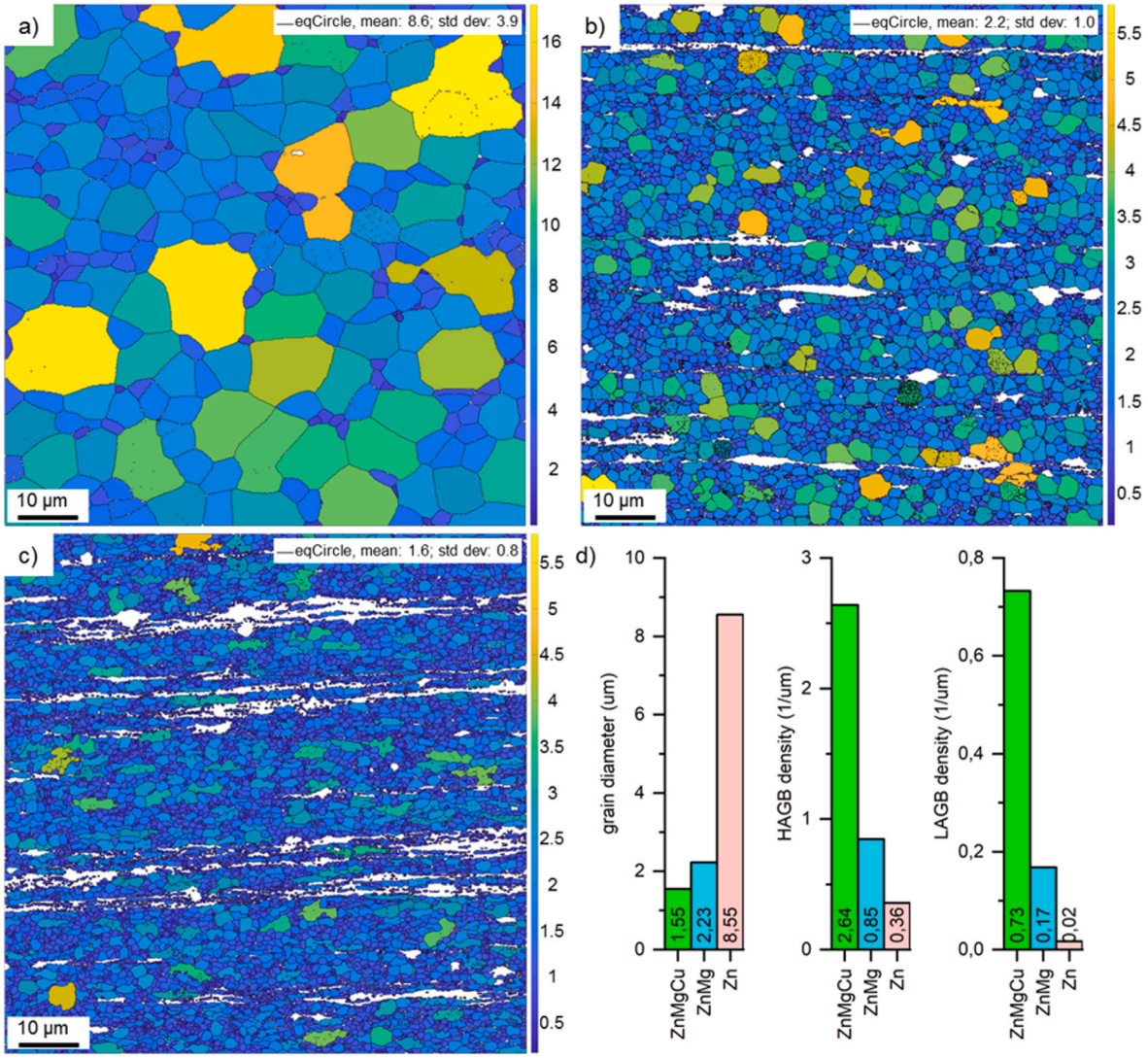

Fig. 2. Grain size distribution maps calculated based on EBSD measurements for a) pure Zn, b) the Zn–Mg alloy and c) the Zn–Mg–Cu alloy after HSE and d) measured values of average grain size and density of HAGB and LAGB.

3. Results

3.1. Microstructure observations

SEM/EBSD observations revealed that all investigated materials possessed a refined microstructure (Fig. 2.). The microstructure of pure Zn after multi-pass HSE in 3 consecutive steps was composed of fine, equiaxed α-Zn grains with an average size of 8.6 ± 4 μm. Alloying additions significantly intensified the effect of grain refinement, as the average grain size, calculated only for the zinc matrix, was 2.2 ± 1 and 1.6 ± 0.8 μm for the Zn–Mg and Zn–Mg–Cu alloys, respectively. Moreover, the maps of grain size distribution indicate that the use of alloying elements led to the formation of a more homogeneous microstructure, with a lower spread of grain size was noticed for Zn–Mg and Zn–Mg–Cu alloys as compared to pure Zn. The grain size distribution map in the case of Zn–Mg–Cu alloy had the most uniform color (blueish), indicating

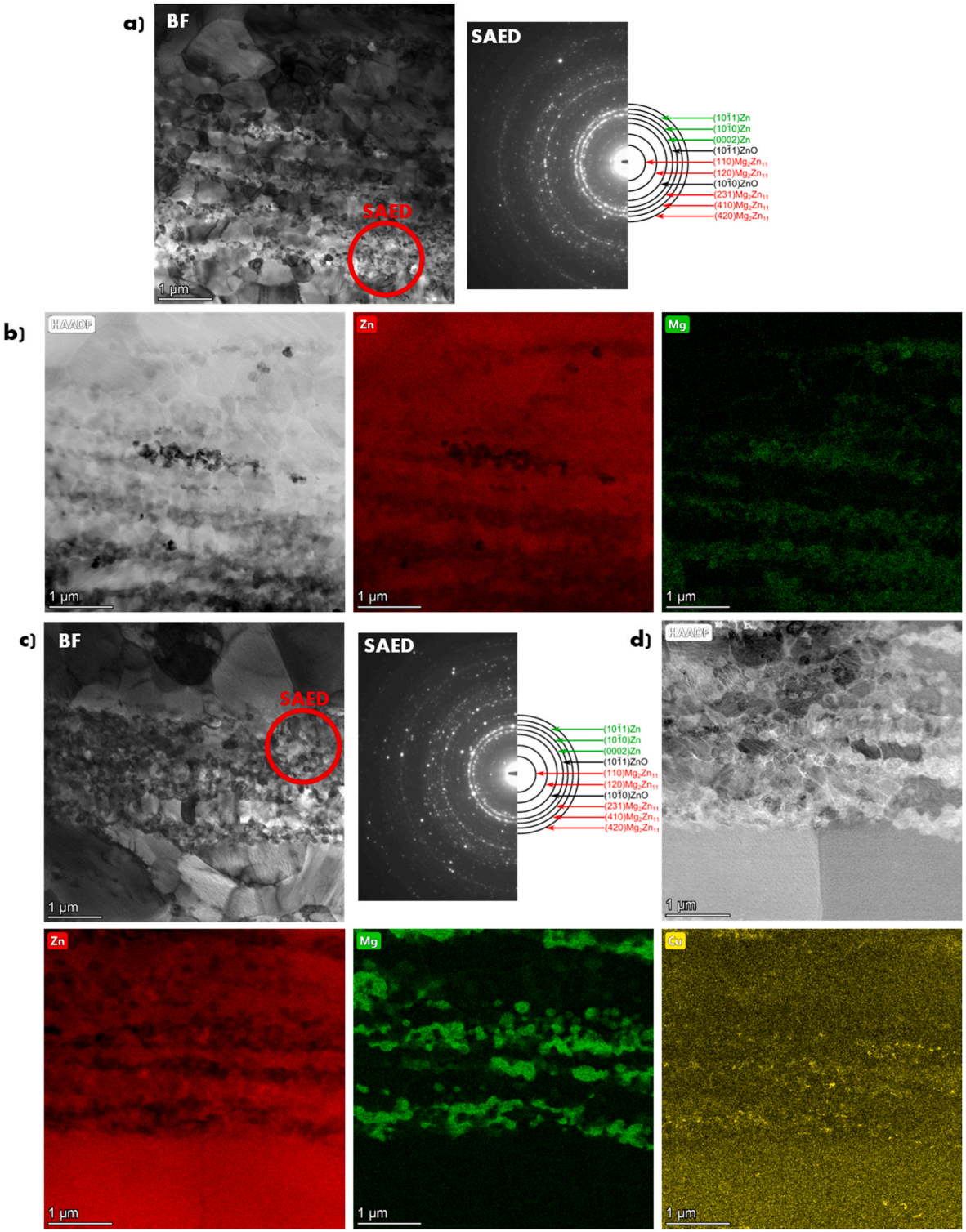

Fig. 3. TEM/BF images together with SAED pattern taken from the regions of the intermetallic phase for a) the Zn–Mg alloy and with corresponding for the alloy map element distribution b) and c), d) for the Zn–Mg–Cu alloy.

that both Mg and Cu addition support the microstructural homogenization. At first sight, the microstructures of both alloys appeared very similar, possessing a band-like character with small equiaxed grains of α-Zn alternating with the eutectic mixture (removed from calculations in Fig. 2) arranged along the ED. It is a detailed, nanoscale TEM/BF microstructure observations coupled with SAED phase analysis that confirmed the presence of the ultra-fine grains of α-Zn and Mg_2Zn_{11} intermetallic phase in the eutectic mixture for both binary and ternary alloys with an emphasis that for Zn–Mg–Cu alloy copper was found to dissolve within η-Zn structure without formation of any other intermetallic phases (according to the EDS chemical analysis) (Fig. 3.). Moreover, it was also observed that alloying substantially affected the substructure formation. With an increasing number of elements, a linear increase in the share of LAGB fraction was noticed. In the case of the ternary alloy, more than 2- and 20-fold increase in the density of the LAGB fraction was calculated as compared to binary alloys and pure Zn, respectively. Based on the SEM/SE observations combined with image analysis, the area fraction of the intermetallic phase was calculated, indicating another difference between the alloys. The binary alloy was characterized by a slightly larger area fraction of the Mg_2Zn_{11}. However, the bands of the intermetallic phase were thinner in comparison with the Zn–Mg–Cu alloy. The calculated parameters describing the intermetallic phase are presented in Table 1.

3.2. Mechanical properties of plastically deformed Zn alloys

Based on static tensile tests, the mechanical properties of the materials were evaluated, and the results are listed in Table 2. The cumulative HSE realized in 3 passes contributed significantly to the strengthening of the materials. The Zn–Mg alloy exhibited the highest values of YS and UTS, reaching 298 MPa and 375 MPa, respectively. Ternary alloys showed similar properties i.e., YS of 262 MPa and UTS of 339 MPa. Obviously, the lowest YS (165 MPa) and UTS (167 MPa) were obtained in the case of pure Zn. However, this material demonstrated the greatest ductility, with an elongation at break assessed at 55%. Both binary and ternary alloys possessed elongation on a comparable level of 30–40 %. The analysis of the stress-strain curves, illustrated in Fig. 4, indicates that pure Zn after HSE is characterized by different mechanical behavior, yet the alloys behave similar. Zn–Mg and Zn–Mg–Cu alloys showed distinct yielding points with a rather low strain hardening effect. A large range of non-uniform strain was observed on stress-strain curves, after which necking occurred. Whereas, in the case of pure Zn, a distinct transition from elastic to plastic region and bigger range of uniform plastic strain were manifested as compared to the alloys.

3.3. Corrosion properties of plastically deformed Zn alloys

Corrosion properties of pure Zn as well as the Zn–Mg and Zn–Mg–Cu alloys were established through both electrochemical and static immersion tests. Fig. 5 shows representative potentiodynamic polarization curves recorded for the investigated materials. Open circuit potential (OCP) and corrosion parameters obtained from potentiodynamic polarization curves: the corrosion potential (E_{corr}), the corrosion current density (j_{corr}), the corrosion rate (CR) and the anodic (b_a) and cathodic (b_c) slopes are listed in Table 3. Regardless of chemical composition, the curves exhibited similar behavior. The cathodic region of all studied materials was almost linear, suggesting that the reaction was controlled by oxygen diffusion [25,26]. On the other hand, the anodic branch was controlled by activation, followed by a sudden increase of the anodic current, which was more pronounced in the case of zinc alloys. This may be associated with the breakdown of the passive layer [27]. Interestingly, the Zn–Mg alloy demonstrated the highest electrochemical potential, the intermediate value was obtained for the Zn–Mg–Cu alloy and the lowest corrosion potential was recorded for pure Zn. Moreover, no direct relation between potential and current density was observed, as seen in Table 3. The differences in current density were negligible. Thus, the calculated corrosion rate stayed on the comparable level.

To further investigate the corrosion behavior of the examined materials, a static immersion test in c-SBF solution for 336 h was conducted. The corrosion rates calculated based on mass loss are consonant with the current densities derived from the potentiodynamic curves and are shown in Fig. 6. No significant differences in corrosion rates between the materials could be noticed. This indicates that neither the presence of the intermetallic phase nor differences in chemical composition between the examined specimens have an impact on their corrosion properties. However, conducted SEM analysis of corrosion layers and material surfaces without corrosion product (after removal with chromic acid) indicate that pure Zn and the alloys possessed different degradation modes. It is clear that it is affected by the intermetallic phase Mg_2Zn_{11} which facilitates the corrosion process. SEM observations revealed that both pure Zn and alloys were covered with a dense layer of corrosion products at the whole surface exposed to the c-SBF solution, however, the alloys exhibited a more pronounced tendency to create agglomerates than pure Zn. We observed a greater diversity of corrosion products for the alloys and different morphologies of the layer (Figs. 7 and 8). The EDS analysis of the corrosion layers performed with the use of FIB cross-sections allowed to detect the presence of Zn, O, Ca, P and Cl in the layer and additionally Mg in case of the alloys (Fig. 8). The distribution maps of elements revealed that Zn and O uniformly covered the area of corrosion product layers, while Ca, P and Mg demonstrated more favored distribution in the form of round-shaped products. This may suggest that initially, ZnO and/or $Zn(OH)_2$ formed on the surface, leading to the formation of different corrosion products containing Ca and P later on. Due to the Mg content in the alloys, the development of $Mg(OH)_2$ was also possible [28]. The creation of a greater number, and more diversified products on the alloys seems reasonable since more corrosion pits were observed on the surface after the removal of corrosion products. SEM observations of the pure Zn surface without corrosion products implied that most of its area stayed intact during immersion and only a few, but rather large pits were present (Fig. 6). This suggests that corrosion is more localized for pure Zn and more uniform for the alloys.

Table 1
Average area fraction and average width of intermetallic phase Mg_2Zn_{11} in the HSE-treated Zn–Mg and Zn–Mg–Cu alloys.

Material	Average area fraction of Mg_2Zn_{11} [%]	Average band width of Mg_2Zn_{11} [μm]
Zn–Mg	13 ± 1	2.3 ± 1
Zn–Mg–Cu	10 ± 1	6.4 ± 4

Table 2
The average values of mechanical properties of plastically deformed pure Zn and the alloys.

Material	YS [MPa]	UTS [MPa]	E [%]
Pure Zn	165 ± 4	167 ± 3	55 ± 2
Zn–Mg	298 ± 6	375 ± 6	35 ± 4
Zn–Mg–Cu	262 ± 17	339 ± 1	36 ± 5

3.4. Cytotoxicity of plastically deformed Zn alloys

Fig. 9 depicts the results coming from the MTT assay performed upon 4-h incubation of cells with zinc extracts. The replacement of normal cell culture media with the those containing metal ions significantly reduced the metabolic activity of cells (100% extracts). In fact, zinc and its alloys tend to greatly affect HUVECs. The only 100% extract that resulted in almost a non-cytotoxic response to endothelial cells was the one taken from Zn–Mg, as indicated by the red dotted line representing the ISO standard for cytotoxicity of materials (i.e., 70%). Interestingly, despite obvious differences in the content of Zn and Zn–Mg–Cu alloys, the

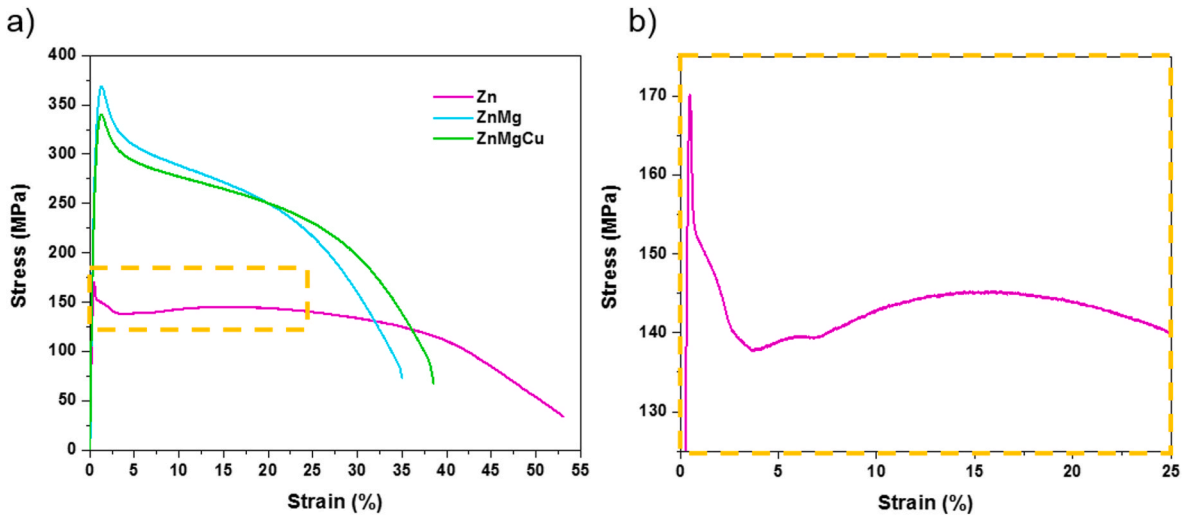

Fig. 4. Stress – strain curves obtained for pure Zn, Zn–Mg and Zn–Mg–Cu alloy after hot extrusion and cumulative hydrostatic extrusion in 3 passes a) and magnified area from pure Zn b)..

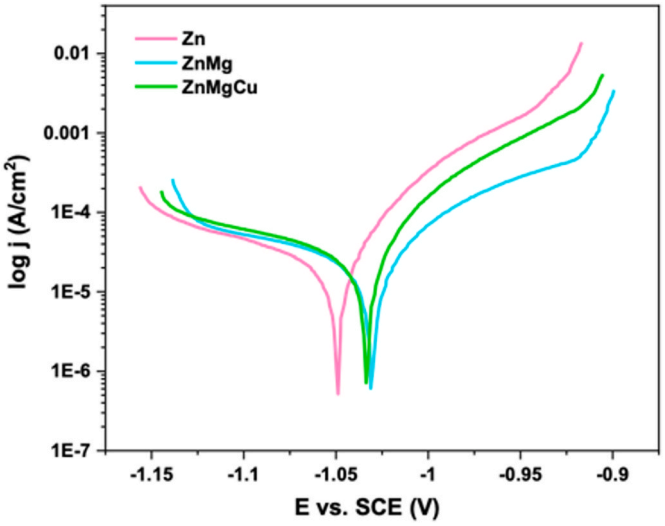

Fig. 5. Representative potentiodynamic curves obtained for pure Zn and the alloys after HSE..

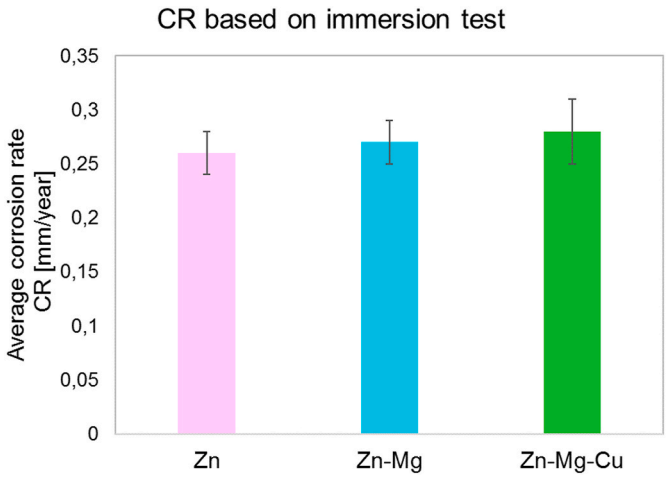

Fig. 6. Corrosion rate obtained for the hydrostatically extruded pure Zn, the Zn–Mg and Zn–Mg–Cu alloys after static immersion test for 336h in c-SBF.

Table 3
Electrochemical parameters of the hydrostatically extruded pure Zn, the Zn–Mg and Zn–Mg–Cu alloys calculated based on the Tafel extrapolation.

Material	OCP [V]	E_{corr} [V]	j_{corr} [μA/cm^2]	CR [mm/year]	b_a [V/dec]	b_c [V/dec]
Pure Zn	−1.034 ± 0.01	−1.044 ± 0.02	31.4 ± 0.2	0.46 ± 0.03	0.06 ± 0.01	0.19 ± 0.03
Zn–Mg	−0.976 ± 0.03	−0.988 ± 0.03	33.2 ± 0.4	0.49 ± 0.06	0.08 ± 0.01	0.25 ± 0.03
Zn–Mg–Cu	−1.019 ± 0.01	−1.026 ± 0.01	36.1 ± 0.1	0.54 ± 0.02	0.08 ± 0.01	0.22 ± 0.02

discrepancies in metabolic activity of cells treated with the respective extracts were statistically insignificant. It may be postulated that once zinc is alloyed with magnesium, cell viability slightly increases. However, additional alloying with copper leads to lowering of cell viability back to the level of pure zinc. This may suggest that magnesium and copper ions have positive and adverse impact on the biocompatibility of zinc, respectively. This observation is even more evident when examining diluted extracts. In the case of 60% extracts, cell viability for Zn–Mg–Cu remained below 70% of control. However, diluted extract positively affected metabolic activity of HUVECs cells and its significant increase for pure Zn up to the level of Zn–Mg alloy was observed. Further dilution of the extract up to 20% resulted in lowering the cytotoxicity of all investigated materials. These findings allow us to conclude that lowering the content of Zn ions results in better metabolic activity of HUVECs cells [29].

The morphologies of zinc treated HUVECs captured with the use of CLSM are depicted in Fig. 10. Exchanging normal cell culture medium with different zinc 100% extracts led to substantial changes in HUVECs' morphology. At first glance, no discrepancies in the number, size and shape of cells were observed while analyzing HUVECs exposed to different zinc 100% extracts. The presence of a monolayer was no longer seen as in the case of the reference sample. Most of the HUVECs were assembled into a characteristic network and a great number of single cells. When it comes to cell morphology, the processes of cytoskeleton condensation as well as nuclei fragmentation were observable. Regardless of the extract type, some HUVECs started to shrink and, at the same time, cellular blebbing occurred. However, despite the considerable impact of zinc extracts on cell morphology, HUVECs exhibiting normal size and shape were also present. Moreover, when analyzing

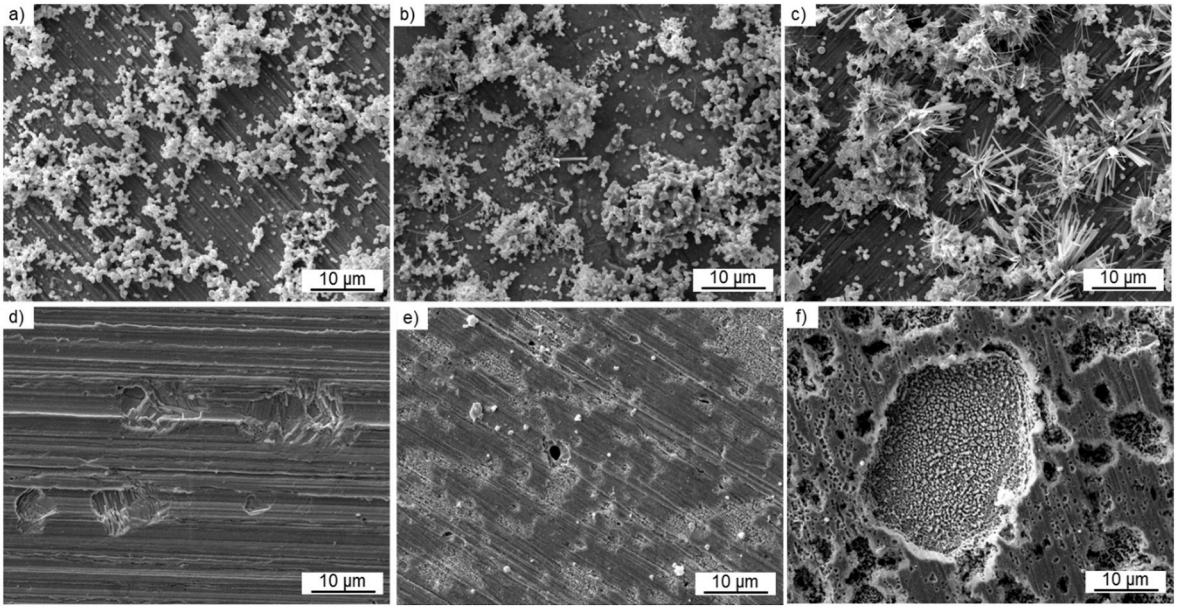

Fig. 7. SEM/SE images of the corrosion products formed after 336h exposition to c-SBF on the surface of the hydrostatically extruded a) pure Zn, b) the Zn–Mg alloy, c) the Zn–Mg–Cu alloy and the corresponding surfaces after removal of corrosion products d), e), f).

morphology of HUVECs exposed to diluted extracts of all investigated materials, the roughly compact monolayer was observed. Overall, the data obtained by confocal imaging is consistent with the MTT assay.

4. Discussion

4.1. Microstructure of plastically deformed Zn alloys

In this work, binary and ternary zinc alloys were prepared and subjected to a two-stage plastic deformation process, composed of hot extrusion, and 3-pass hydrostatic extrusion. Characterization of the material including microstructure, mechanical, corrosion and biological properties, aimed at finding correlation between microstructure and performance of heavily deformed zinc-based materials.

EBSD measurements revealed that the microstructure exhibited typical characteristics of HSE-treated zinc-based alloys [30]. Significant grain refinement as well as the increase of structural defects were observed [10]. Reduction of the number of HSE passes, while maintaining the same true strain ($\varepsilon = 3.6$) did not induce notable changes in the microstructure. For instance, in the case of Zn–1Mg after 4-passes of HSE, an average grain size of 1.5 μm was achieved for Zn–1Mg alloy [10], whereas with 3-passes HSE for Zn-0.8 Mg, a grain size of 2.2 μm was obtained. Moreover, similarity can also be found in behavior of the intermetallic phase, where 3-passes are also enough to fragment the Mg_2Zn_{11} phase and arrange it into elongated bands along the extrusion direction [12]. When comparing our results obtained for Zn–Mg alloy with other SPD techniques, the ECAP process can be more efficient in the reduction of grain size as average values of 1.1–1.4 μm were obtained [8,31]. The best grain refinement was achieved by HPT, where for Zn–1Mg alloys the average grain size was 0.9 μm [9].

The minor addition of copper to the Zn–Mg alloys resulted in better grain refinement with more homogeneous microstructure in terms of grain size and significantly higher amount of LAGBs as compared to pure Zn and binary alloys (about 20 and 2 times, respectively). This suggests that solute copper within the matrix contributes to an increase of recrystallization temperature and thus lowering the impact of dynamic recrystallization during the HSE deformation process, allowing to preserve smaller grain size with increased number of structural defects. Similar results, indicating that copper may have an impeding effect on dynamic recrystallization and thus grain growth, were presented in Ref. [16]. A heterogeneous microstructure composed of equiaxed and elongated grains with a large number of LAGBs was achieved during cold rolling. Moreover, the addition of copper into Zn–Mg affected interaction between the matrix and intermetallic, resulting in a more heterogeneous distribution of bands of Mg_2Zn_{11}. This was evidenced by measured values of bandwidth. In the case of Zn–Mg–Cu alloy, wider bands with a greater standard deviation from the average value, as compared with binary alloy were obtained. Comparable results were obtained for ECAP-treated Zn–3Cu-0.5 Mg alloy, where the distribution of bands of intermetallic phase was not uniform [32].

4.2. Microstructural relation with mechanical properties

Significant grain refinement provided by hydrostatic extrusion executed in 3 consecutive passes contributed to the strengthening of the Zn-based materials. Decreasing the number of HSE passes had an especially beneficial impact on pure Zn, where higher YS and UTS were observed as compared to 4-passes [10], what can be ascribed to smaller grain size obtained in the present work. Those results are superior to the other SPD methods like ECAP [33] or HPT [34].

Considering the Hall-Petch relationship, the theoretical contribution of grain boundary strengthening can be calculated. Based on the formula [35], the estimated values of grain boundary strengthening were 103 MPa, 201 MPa and 241 MPa, respectively for pure Zn, Zn–Mg alloy and Zn–Mg–Cu alloy. The obtained theoretical value was the closest to the measured one for pure Zn (165 MPa). So, it can be assumed that grain refinement obtained via HSE is the main factor responsible for strengthening of the materials.

Modified microstructure due to the addition of Mg led to meaningful improvement of the material achieving the highest mechanical properties among investigated materials (YS of 298 MPa, UTS of 375 MPa and E of 35%). Those results, (as opposed to pure Zn) indicated lower strength than those obtained by 4-passes HSE (YS of 383 MPa, UTS of 482 MPa) [10]. However, better plasticity of Zn–Mg alloys can be achieved in 3- than 4-passes of HSE [10]. This is probably due to weakening of the texture [36,37].

Interestingly in Zn–Mg–Cu alloys, higher stored energy due to greater density of high and low angle grain boundaries did not contribute to a better strengthening effect of ternary alloys as compared to binary alloys. However, this effect is diminished by the less uniform

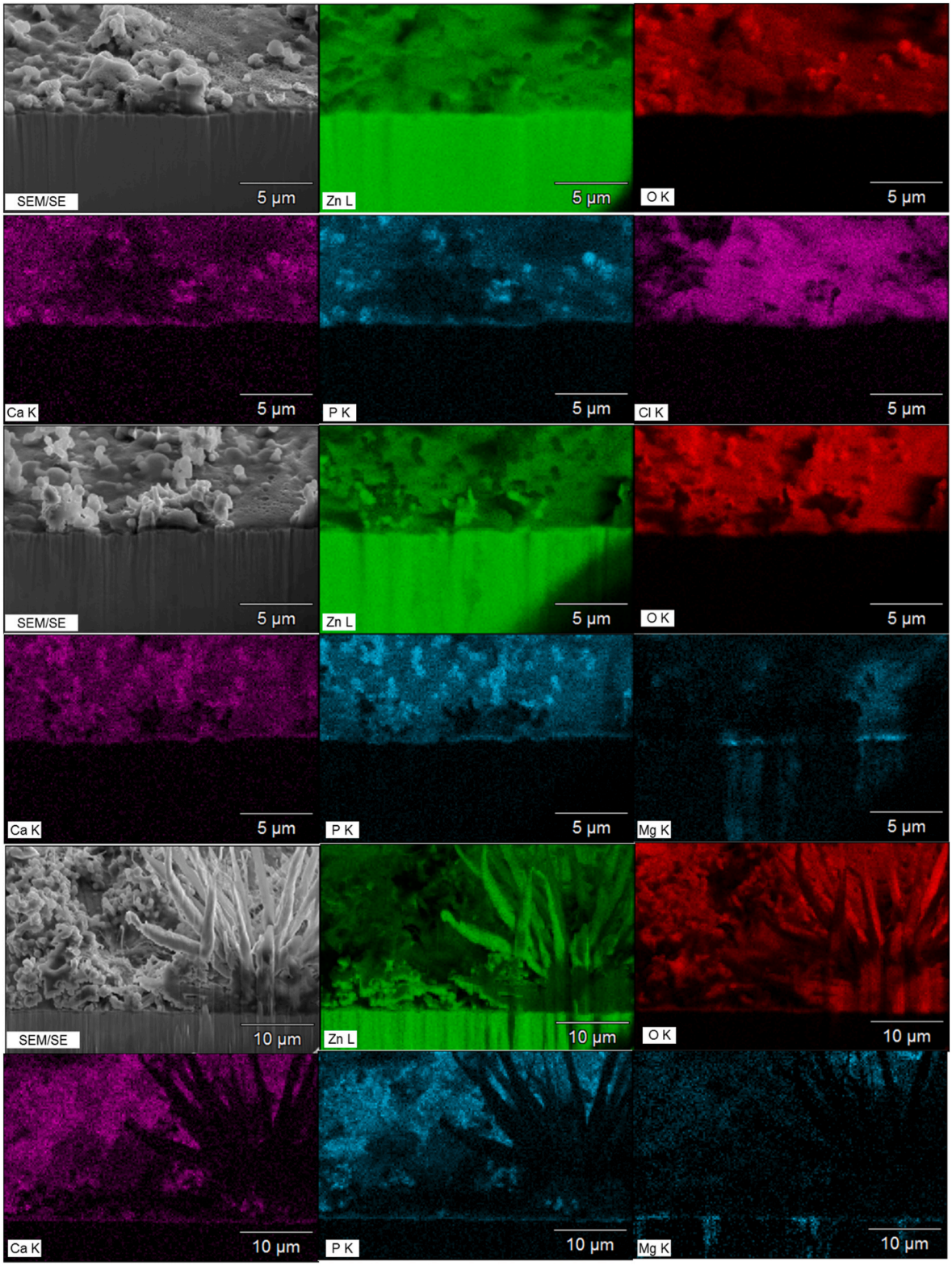

Fig. 8. Element distribution in the corrosion layer formed after 336h exposition to c-SBF obtained from FIB cross-sections of the hydrostatically extruded a) pure Zn, b) Zn–Mg alloys and c) Zn–Mg–Cu alloys.

distribution of intermetallic phase in the case of the Zn–Mg–Cu alloys, where wider bands constitute larger obstacles to dislocation movement, thus impeding plastic deformation [4].

4.3. Microstructural relation with corrosion properties

Results showed that grain refinement observed in all materials contributed to better corrosion resistance, since regardless of the materials chemical composition the corrosion rate stayed on a similar level. An increased number of grain boundaries can act as a physical barrier for

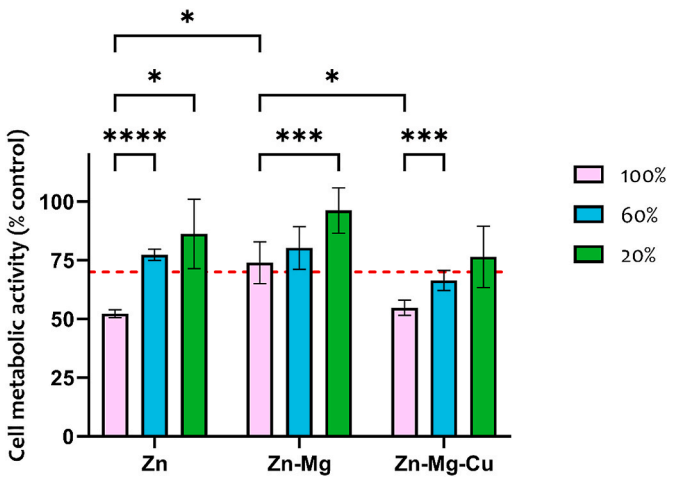

Fig. 9. Metabolic activities of HUVECs exposed to different zinc extracts.

corrosion and can facilitate formation of a protective dense film [19,38,39]. This can be supported by the higher corrosion potential for both alloys compared to pure Zn, where the average grain size was about 4 times smaller for the alloys [40]. Fragmentation and uniform distribution of Mg_2Zn_{11} within the material can also be responsible for the improvement of corrosion potential of the Zn–Mg alloy as compared to the other investigated materials [20,41]. Ye et al. also emphasized the significance of microstructure in corrosion behavior. The authors proved that the corrosion potential and hence degradation rate is dependent on grain size and amount of intermetallic phase [19].

However, the corrosion mode of the investigated materials varied based on their chemical composition. SEM observations including EDS analysis revealed different chemical composition of the corrosion layer. More diverse corrosion products were presented on the alloys' surface, suggesting, not only the Zn, but also Mg ions release (Fig. 8) [42]. Moreover, it is also consistent with SEM analysis of the surface without corrosion products. With an increased number of alloying additions, an enlarged number of pits was observed. This is due to the intermetallic phase presence in the microstructure with a different corrosion potential than the matrix. Thus, micro-galvanic corrosion occurred, initiating material degradation. Moreover, a larger number of corrosion products and pits for Zn–Mg–Cu alloy can be related to a more pronounced difference in electrochemical potential between the matrix and intermetallic phase. More positive potential of the Zn–Mg–Cu matrix is attributed to the solute copper within it [43]. Despite an enlarged number of pits on the surface of the alloys, they were distributed evenly on the surface indicating more uniform corrosion, than in pure zinc. On the other hand, deep, isolated pits were present on the corroded surface of the pure Zn (seen after corrosion products removal, Fig. 7d). Similar observations were achieved by Ref. [44], where pure Zn exhibited localized corrosion related to microstructure. Such localized corrosion in pure Zn could be related to crystallographic texture, where some privileged orientation initiates the corrosion process. Due to this localized corrosion causing substantial mass loss of pure Zn, its degradation rate and Zn-based alloys processed by HSE remain on a comparable level.

Our studies suggest that corrosion properties depend on microstructural features, which may superimpose, when heavy plastic deformation is applied and make it difficult to distinguish the leading cause affecting corrosion properties, hence requires further investigations.

4.4. *Effect of zinc ions on biocompatibility*

Although, it is difficult to find a direct link between microstructure and biological response of Zn-based materials, since the experiments are typically carried out with the use of zinc extracts, some possible relations with the chemical composition can be found and are proposed based on the conducted studies. Generally, it is proved that [45] zinc ions reduce cell viability. Hence, by tailoring chemical composition, the ion release may be controlled [46] The addition of alloying elements (forming solid solution with Zn and/or the secondary phases) may alter the release of ions from biodegradable samples. As a result, the total

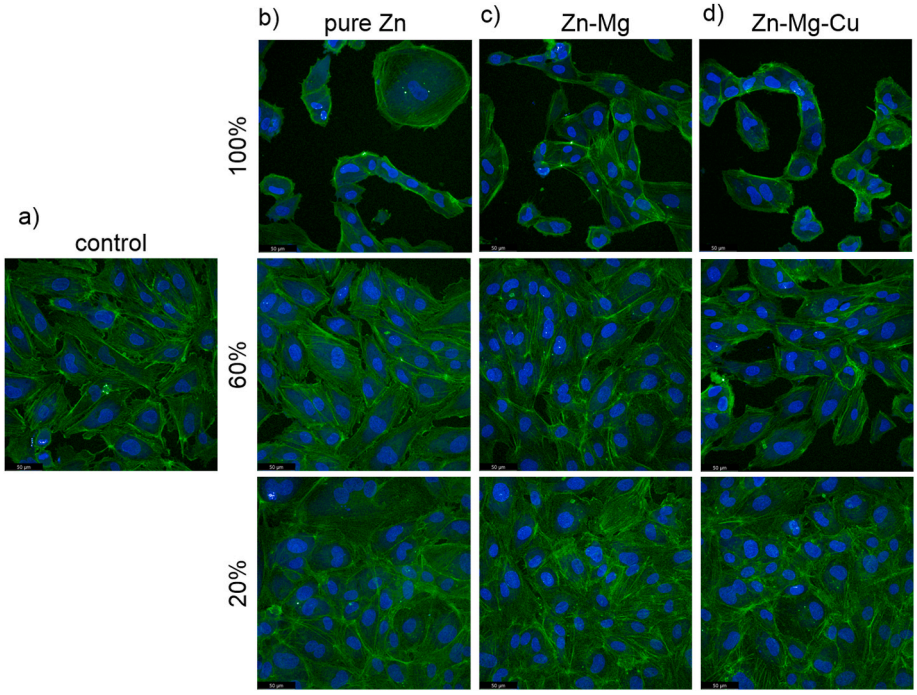

Fig. 10. CLSM-derived morphologies of HUVECs a) control, and incubated for 4 h with different extracts harvested from b) pure Zn, c) Zn–Mg alloy and d) Zn–Mg–Cu alloy. The cell nuclei and filamentous actin of the cytoskeleton were stained with the use of DAPI (blue color) and FITC-phalloidin (green color), respectively. (For interpretation of the references to color in this figure legend, the reader is referred to the Web version of this article.)

amount of released Zn^{2+} decreases in favor of the ions from alloying elements that may have a positive impact on biocompatibility of the material. The statement is supported by our finding, where the Zn–Mg alloy elicited almost non-cytotoxic effect on endothelial cells as opposed to pure Zn and Zn–Mg–Cu alloys. This correlates well with results derived from corrosion tests. In the corrosion layer, formed on the HSE-treated zinc alloys, some products containing Mg were observed. Hence, the presence of Mg ions in the zinc extracts is possible despite low Mg content in the alloy [47]. Mg is known to exhibit excellent biocompatibility [48]. Thus, it may lower the cytotoxicity of Zn alloy [46] Interestingly, the addition of Cu into Zn–Mg decreased cell viability back to the level of pure Zn. It is probably due to possible Cu ion release, which could have a negative impact on cell viability. Huang et al. detected Cu-containing corrosion products on the surface of Zn–Cu–Li alloy and observed decrease in viability below the accepted threshold for 100% zinc extracts [43]. In our studies we did not distinguish any corrosion products bearing Cu, what may be in fact related to the small amount of this element in the alloy, being below the limitation of the EDS method. Some other reports also showed the adverse effect of Cu on cell viability in 100% extracts for various alloys of different chemical composition e.g., Zn-Cu-Fe [32,41,49].

Our findings coincide with the trends observed in the literature, as 100% zinc extracts generally lead to lowest cell viability [21]. For example, Xu et al. examined different cell lines including murine macrophages, HUVECs and mouse pre-osteoblasts and in all cases, the 100% extracts severely aggravated cell viability [41]. On the other hand, in all these cultures, when extracts got diluted, better cell response was observed. It is in accordance with our result, where a correlation between extract dilution and cytotoxicity was noticed. The lower the concentration of zinc ions in the extracts, the better metabolic activity of the endothelial cells was obtained.

Even though we have observed moderate cytotoxicity in the case of 100% extracts for both Zn and Zn–Mg–Cu alloys, the CLSM studies revealed no differences between all of the analyzed materials when it comes to cell morphology. A lot of cells of round shape and blebs were observed in addition to “cobblestone”-like endothelial cells for all of the tested cultures. However, once the extracts were diluted, the almost a complete monolayer was achieved for all investigated materials. This also implies positive effect of lowering zinc ions concentration on better biocompatibility of the zinc-based materials.

5. Conclusions

Carried out comprehensive analysis of HSE-processed Zn-based alloys allowed to conclude that:

1. Alloying addition can enhance grain refinement achieved by plastic deformation via HSE. The smallest average grain size, reaching 1.6 μm was obtained for the Zn–Mg–Cu alloy. This result can be attributed to the formation of the Mg_2Zn_{11} intermetallic phase and an increased recrystallization temperature due to the presence of Cu in solid solution within the matrix.
2. Three consecutive passes of HSE are sufficient to provide the mechanical strength of Zn alloys due to refinement of grain size and intermetallic phase, which exceeds the design requirements for absorbable implants.
3. HSE combined with alloying additions did not adversely affect the corrosion rate, as it remained within a similar range for all investigated materials. Moreover, HSE contributed to more homogeneous degradation of the alloys.
4. Alloying also influenced a different corrosion mode, which could affect biological properties by releasing Mg ions while simultaneously decreasing the release rate of Zn ions. This resulted in a slightly improved cell viability for the Zn–Mg alloy compared to pure Zn material.

In summary, hydrostatic extrusion is a suitable method for producing high-strength materials with uniform degradation and sufficient biocompatibility, once the chemical composition of the alloy will be carefully selected. Thus, the HSE-treated zinc alloys can be a promising candidate for producing absorbable implants.

Declaration of competing interest

The authors declare that they have no known competing financial interests or personal relationships that could have appeared to influence the work reported in this paper.

Acknowledgements

The authors acknowledge financial support from the National Center for Research and Development, Warsaw, Poland project no. LIDER/54/0229/L-11/19/NCBR/2020. The authors would like to thank the UMCG Endothelial Cell facility for providing the cells to be used for the biological experiments.

References

[1] Zhuo X, et al. Recent progress of novel biodegradable zinc alloys: from the perspective of strengthening and toughening. J Mater Res Technol 2022;17:244–69. https://doi.org/10.1016/j.jmrt.2022.01.004.
[2] Costa MI, Sarmento-Ribeiro AB, Gonçalves AC. Zinc: from biological functions to therapeutic potential. Int J Mol Sci 2023;24(5):4822. https://doi.org/10.3390/ijms24054822.
[3] Mostaed E, Sikora-Jasinska M, Drelich JW, Vedani M. Zinc-based alloys for degradable vascular stent applications. Acta Biomater 2018;71:1–23. https://doi.org/10.1016/j.actbio.2018.03.005.
[4] Huang H, et al. Recent advances on the mechanical behavior of zinc based biodegradable metals focusing on the strain softening phenomenon. Acta Biomater 2022;152:1–18. https://doi.org/10.1016/j.actbio.2022.08.041.
[5] Mollaei N, Razavi SH, Aboutalebi MR, Fatemi SM. Effect of Mn addition on the microstructure, mechanical, and corrosion properties of an extruded biodegradable Zn-0.2Mg alloy. J Mater Res Technol 2023;22:1983–98. https://doi.org/10.1016/j.jmrt.2022.12.049.
[6] Ardakani MS, Mostaed E, Sikora-Jasinska M, Kampe SL, Drelich JW. The effects of alloying with Cu and Mn and thermal treatments on the mechanical instability of Zn-0.05Mg alloy. Mater Sci Eng, A 2020;770:138529. https://doi.org/10.1016/j.msea.2019.138529.
[7] Luqman M, Ali Y, Zaghloul MMY, Sheikh FA, Chan V, Abdal-hay A. Grain refinement mechanism and its effect on mechanical properties and biodegradation behaviors of Zn alloys – a review. J Mater Res Technol 2023;24:7338–65. https://doi.org/10.1016/j.jmrt.2023.04.219.
[8] Ye L, et al. Achieving high strength, excellent ductility, and suitable biodegradability in a Zn-0.1Mg alloy using room-temperature ECAP. J Alloys Compd 2022;926:166906. https://doi.org/10.1016/j.jallcom.2022.166906.
[9] Martynenko N, et al. Structure, biodegradation, and in vitro bioactivity of Zn–1% Mg alloy strengthened by high-pressure torsion. Materials 2022;15(24):9073. https://doi.org/10.3390/ma15249073.
[10] Jarzębska A, et al. Controlled grain refinement of biodegradable Zn-Mg alloy: the effect of magnesium alloying and multi-pass hydrostatic extrusion preceded by hot extrusion. Metall Mater. Trans. A Phys. Metall. Mater. Sci. 2020;51(12):6784–96. https://doi.org/10.1007/s11661-020-06032-4.
[11] Pachla W, et al. Structural and mechanical aspects of hypoeutectic Zn–Mg binary alloys for biodegradable vascular stent applications. Bioact Mater 2021;6(1):26–44. https://doi.org/10.1016/j.bioactmat.2020.07.004.
[12] Jarzębska A, et al. A new approach to plastic deformation of biodegradable zinc alloy with magnesium and its effect on microstructure and mechanical properties. Mater Lett 2018;211:58–61. https://doi.org/10.1016/j.matlet.2017.09.090.
[13] Faraji G, Kim HS. Review of principles and methods of severe plastic deformation for producing ultrafine-grained tubes. Mater Sci Technol 2017;33(8):905–23. https://doi.org/10.1080/02670836.2016.1215064.
[14] Kabir H, Munir K, Wen C, Li Y. Recent research and progress of biodegradable zinc alloys and composites for biomedical applications: biomechanical and biocorrosion perspectives. Bioact Mater 2021;6(3):836–79. https://doi.org/10.1016/j.bioactmat.2020.09.013.
[15] Wang L, et al. Effect of cumulative strain on the microstructural and mechanical properties of Zn-0.02 wt%Mg alloy wires during room-temperature drawing process. J Alloys Compd 2018;740:949–57. https://doi.org/10.1016/j.jallcom.2018.01.059.
[16] Jarzębska A, et al. Dynamic recrystallization and its effect on superior plasticity of cold-rolled bioabsorbable zinc-copper alloys. Materials 2021;14(13):3483. https://doi.org/10.3390/ma14133483.
[17] Luqman M, Ali Y, Zaghloul MMY, Sheikh FA, Chan V, Abdal-hay A. Grain refinement mechanism and its effect on mechanical properties and biodegradation

behaviors of Zn alloys – a review. J Mater Res Technol 2023;24:7338–65. https://doi.org/10.1016/j.jmrt.2023.04.219.
[18] Ralston KD, Birbilis N. Effect of grain size on corrosion: a review. 75005-075005–13 Corrosion 2010;66(7). https://doi.org/10.5006/1.3462912.
[19] Ye L, et al. Effect of grain size and volume fraction of eutectic structure on mechanical properties and corrosion behavior of as-cast Zn–Mg binary alloys. J Mater Res Technol 2022;16:1673–85. https://doi.org/10.1016/j.jmrt.2021.12.101.
[20] Guo P, et al. Ultrafine- and uniform-grained biodegradable Zn-0.5Mn alloy: grain refinement mechanism, corrosion behavior, and biocompatibility in vivo. Mater Sci Eng C 2021;118:111391. https://doi.org/10.1016/j.msec.2020.111391.
[21] Venezuela J, Dargusch MS. The influence of alloying and fabrication techniques on the mechanical properties, biodegradability and biocompatibility of zinc: a comprehensive review. Acta Biomater 2019;87:1–40. https://doi.org/10.1016/j.actbio.2019.01.035.
[22] Guillory RJ, et al. Improved biocompatibility of Zn–Ag-based stent materials by microstructure refinement. Acta Biomater 2022;145:416–26. https://doi.org/10.1016/j.actbio.2022.03.047.
[23] www.crystorient.com accessed: October.16, 2023.
[24] Oyane A, Kim H, Furuya T, Kokubo T, Miyazaki T, Nakamura T. Preparation and assessment of revised simulated body fluids. J Biomed Mater Res 2003;65A(2):188–95. https://doi.org/10.1002/jbm.a.10482.
[25] Kubásek J, Dvorský D, Čapek J, Pinc J, Vojtěch D. Zn-Mg biodegradable composite: novel material with tailored mechanical and corrosion properties. Materials 2019;12(23):3930. https://doi.org/10.3390/ma12233930.
[26] Vida TA, Soares T, Septimio RS, Brito CC, Cheung N, Garcia A. Effects of macrosegregation and microstructure on the corrosion resistance and hardness of a directionally solidified Zn-5.0wt.%Mg alloy. Mater Res 2019;22(suppl 1). https://doi.org/10.1590/1980-5373-mr-2019-0009.
[27] Guo P, et al. Corrosion characteristics of zinc–zirconium alloy in c-SBF and its biocompatibility in vitro/in vivo. Mater Corros 2020;71(2):196–208. https://doi.org/10.1002/maco.201911137.
[28] Alves MM, Prošek T, Santos CF, Montemor MF. Evolution of the in vitro degradation of Zn–Mg alloys under simulated physiological conditions. RSC Adv 2017;7(45):28224–33. https://doi.org/10.1039/C6RA28542B.
[29] Wojtas D, et al. Quantum sensing for detection of zinc-triggered free radicals in endothelial cells. Adv. Quantum. Technol. 2023;6(11). https://doi.org/10.1002/qute.202300174.
[30] Jarzębska A, et al. Synergistic effect of Mg addition and hydrostatic extrusion on microstructure and texture of biodegradable low-alloyed zinc. IOP Conf Ser Mater Sci Eng 2018;375:012008. https://doi.org/10.1088/1757-899X/375/1/012008.
[31] Wang X, Ma Y, Meng B, Wan M. Effect of equal-channel angular pressing on microstructural evolution, mechanical property and biodegradability of an ultrafine-grained zinc alloy. Mater Sci Eng, A 2021;824:141857. https://doi.org/10.1016/j.msea.2021.141857.
[32] Liu H, et al. Evolutions of CuZn5 and Mg2Zn11 phases during ECAP and their impact on mechanical properties of Zn–Cu–Mg alloys. J Mater Res Technol 2022;21:5032–44. https://doi.org/10.1016/j.jmrt.2022.11.095.
[33] Bednarczyk W, Wątroba M, Kawałko J, Bała P. Can zinc alloys be strengthened by grain refinement? A critical evaluation of the processing of low-alloyed binary zinc alloys using ECAP. Mater Sci Eng, A 2019;748:357–66. https://doi.org/10.1016/j.msea.2019.01.117.
[34] Srinivasarao B, Zhilyaev AP, Langdon TG, Pérez-Prado MT. On the relation between the microstructure and the mechanical behavior of pure Zn processed by high pressure torsion. Mater Sci Eng, A 2013;562:196–202. https://doi.org/10.1016/j.msea.2012.11.027.
[35] Wojtas D, et al. Microstructure-strength relationship of ultrafine-grained titanium manufactured by unconventional severe plastic deformation process. J Alloys Compd 2020;837:155576. https://doi.org/10.1016/j.jallcom.2020.155576.
[36] Li R, Ding Y, Zhang H, Lei J, Shen Y. Effective strengthening and toughening in Zn-1mg alloy with bimodal grain structure achieved by conventional extrusion. SSRN Electron J 2022. https://doi.org/10.2139/ssrn.4117397.
[37] Guo P, et al. Ultra-fine-grained Zn-0.5Mn alloy processed by multi-pass hot extrusion: grain refinement mechanism and room-temperature superplasticity. Mater Sci Eng, A 2019;748:262–6. https://doi.org/10.1016/j.msea.2019.01.089.
[38] Chung M-K, Choi Y-S, Kim J-G, Kim Y-M, Lee J-C. Effect of the number of ECAP pass time on the electrochemical properties of 1050 Al alloys. Mater Sci Eng, A 2004;366(2):282–91. https://doi.org/10.1016/j.msea.2003.08.056.
[39] Huang T, Liu Z, Wu D, Yu H. Microstructure, mechanical properties, and biodegradation response of the grain-refined Zn alloys for potential medical materials. J Mater Res Technol 2021;15:226–40. https://doi.org/10.1016/j.jmrt.2021.08.024.
[40] Huang H, et al. A high-strength and biodegradable Zn–Mg alloy with refined ternary eutectic structure processed by ECAP. Acta Metall Sin 2020;33(9):1191–200. https://doi.org/10.1007/s40195-020-01027-x.
[41] Xu Y, et al. Biodegradable Zn-Cu-Fe alloy as a promising material for craniomaxillofacial implants: an in vitro investigation into degradation behavior, cytotoxicity, and hemocompatibility. Front Chem 2022;10. https://doi.org/10.3389/fchem.2022.860040.
[42] Pinc J, et al. A detailed mechanism of degradation behaviour of biodegradable as-ECAPed Zn-0.8Mg-0.2Sr with emphasis on localized corrosion attack. Bioact Mater 2023;27:447–60. https://doi.org/10.1016/j.bioactmat.2023.04.012.
[43] Huang S, Wang L, Zheng Y, Qiao L, Yan Y. In vitro degradation behavior of novel Zn–Cu–Li alloys: roles of alloy composition and rolling processing. Mater Des 2021;212:110288. https://doi.org/10.1016/j.matdes.2021.110288.
[44] Yue R, et al. Effects of extrusion temperature on microstructure, mechanical properties and in vitro degradation behavior of biodegradable Zn-3Cu-0.5Fe alloy. Mater Sci Eng C 2019;105:110106. https://doi.org/10.1016/j.msec.2019.110106.
[45] Wątroba M, et al. In vitro cytocompatibility and antibacterial studies on biodegradable Zn alloys supplemented by a critical assessment of direct contact cytotoxicity assay. J Biomed Mater Res B Appl Biomater 2023;111(2):241–60. https://doi.org/10.1002/jbm.b.35147.
[46] Tang Z, et al. Design and characterizations of novel biodegradable Zn-Cu-Mg alloys for potential biodegradable implants. Mater Des 2017;117:84–94. https://doi.org/10.1016/j.matdes.2016.12.075.
[47] Ramirez–Ledesma AL, et al. Introducing novel bioabsorbable Zn–Ag–Mg alloys intended for cardiovascular applications. Mater Today Commun 2023;35:105544. https://doi.org/10.1016/j.mtcomm.2023.105544.
[48] Bairagi D, Mandal S. A comprehensive review on biocompatible Mg-based alloys as temporary orthopaedic implants: current status, challenges, and future prospects. J Magnesium Alloys 2022;10(3):627–69. https://doi.org/10.1016/j.jma.2021.09.005.
[49] Wei Z, et al. Impact of copper on corrosion behavior, biocompatibility and antibaterial activity of biodegradable Zn-3Mg-xCu alloys for orthopedic applications. Mater Res Express 2023;10(9):095401. https://doi.org/10.1088/2053-1591/acf6af.